Electronic Supplementary Material (ESI) for Dalton Transactions.

Supporting Information to accompany

Tuning Valence Tautomerism in a Family of Dinuclear Cobalt Complexes Incorporating a Conjugated Bridging Bis(dioxolene) Ligand with Weak Communication

Tristan E. Fischer, Jett T. Janetzki, F. Zahra M. Zahir, Robert W. Gable, Alyona A. Starikova and Colette Boskovic*

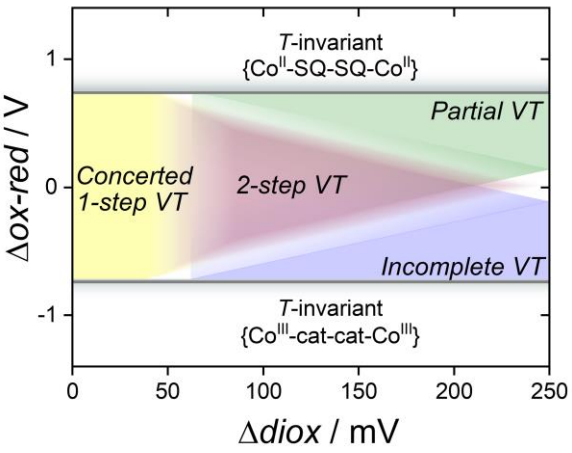

Fig S1 Correlation between redox parameters and VT transition profile for dinuclear cobalt complexes bridged by a bis(dioxolene) ligand established by Gransbury, Boskovic *et. al*.[1] Figure adapted with permission from G. K. Gransbury, B. N. Livesay, J. T. Janetzki, M. A. Hay, R. W. Gable, M. P. Shores, A. Starikova and C. Boskovic, *J. Am. Chem. Soc.*, 2020, **142**, 10692–10704. Copyright 2020 American Chemical Society.

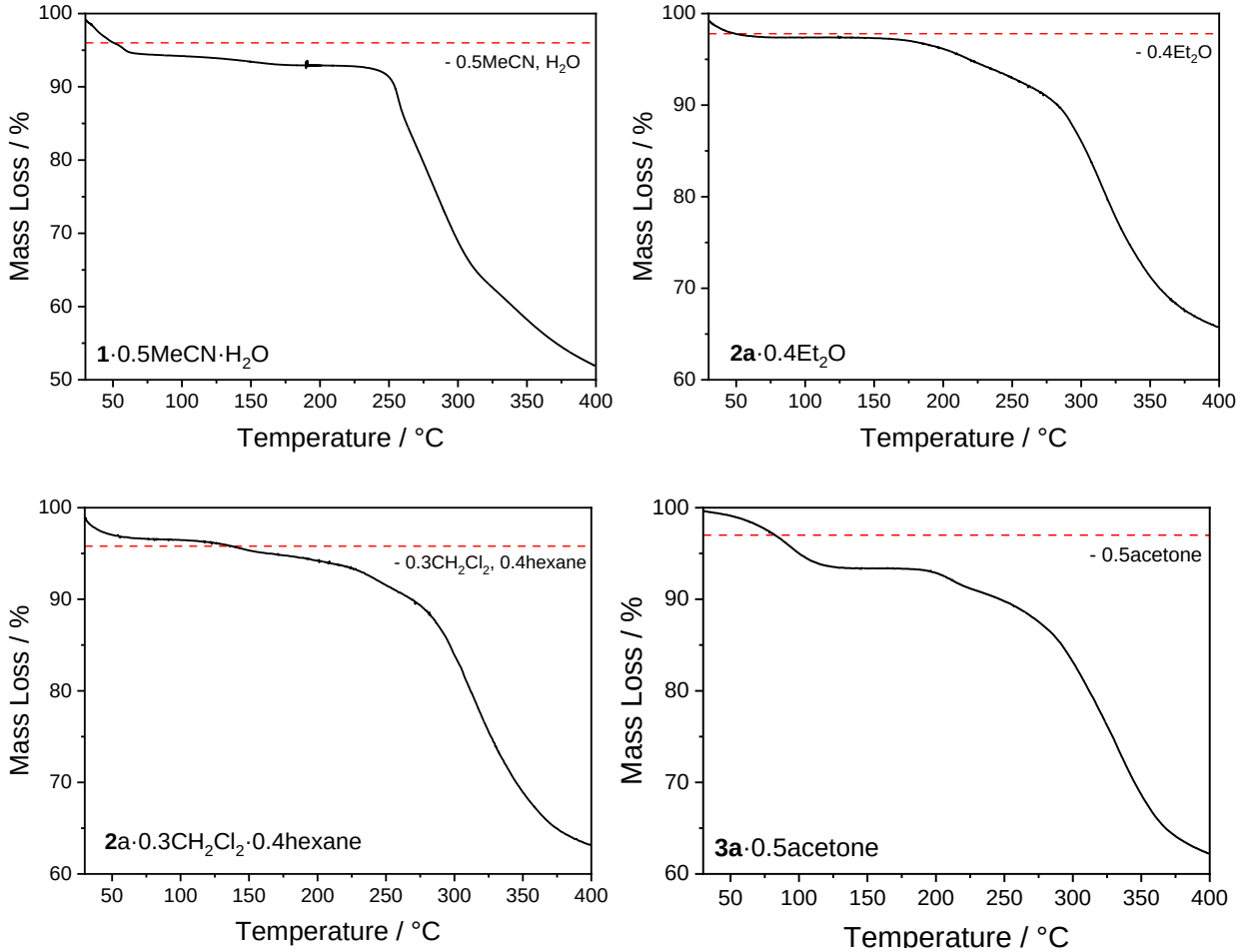

Fig S2 Thermogravimetric profile for **1a**·0.5MeCN·H_2O, **2a**·0.4Et_2O, **2a**·0.3CH_2Cl_2·0.4hexane, and **3a**·0.5acetone at a ramp rate of 5 °C min^{-1}.

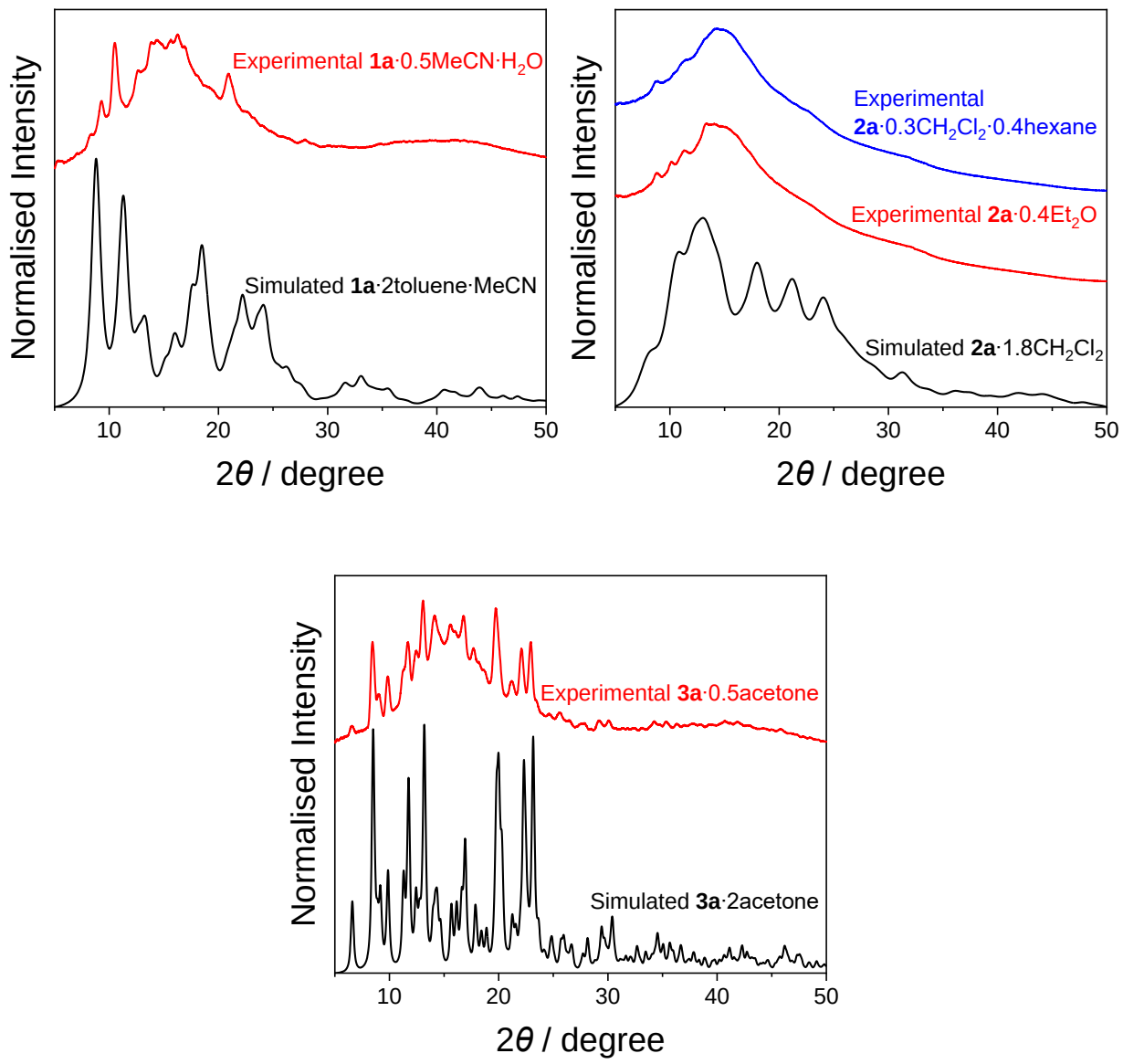

Fig S3 Top left: Experimental PXRD pattern for **1a**·0.5MeCN·H_2O and simulated PXRD pattern for **1a**·2toluene·MeCN**.** Top right: Experimental PXRD pattern for **2a**·0.4Et_2O and **2a**·0.3CH_2Cl_2·0.4hexane, and simulated PXRD pattern for **2a**·1.8CH_2Cl_2. Bottom: Experimental PXRD pattern for **3a**·0.5acetone, and simulated PXRD pattern for **3a**·2acetone.

Table S1 Crystallographic data and structure refinement parameters for compounds **1a**·2toluene·2MeCN, **2a**·1.8CH_2Cl_2, and **3a**·2acetone collected at 100 K.

	1a·2toluene·2MeCN	**2a**·1.8CH_2Cl_2	**3a**·2acetone
Empirical formula	$C_{70}H_{70}Co_2F_{12}N_{12}O_6P_2$	$C_{57.8}H_{57.6}Cl_{3.6}Co_2F_{12}N_{10}O_6P_2$	$C_{64}H_{72}Co_2F_{12}N_{10}O_8P_2$
Formula weight	1583.18	1523.76	1517.11
Temperature (K)	99.0(1)	100.0(2)	100.0(2)
Crystal system	triclinic	monoclinic	monoclinic
Space group	*P*-1	$P2_1/n$	$P2_1/n$
a (Å)	8.6957(2)	10.813(2)	15.396(3)
b (Å)	10.8984(2)	13.371(3)	13.874(3)
c (Å)	20.7669(4)	22.478(5)	16.953(3)
α (°)	93.436(2)	90	90
β (°)	101.986(2)	103.68(3)	112.52(3)
γ (°)	111.088(2)	90	90
Volume (Å^3)	1776.57(7)	3157.7(12)	3345.1(13)
Z	1	2	2
ρ_{calc} (g/cm^3)	1.480	1.603	1.506
μ (mm^{-1})	4.884	0.823	0.639
F(000)	814.0	1551.0	1564.0
Crystal size (mm^3)	0.276 × 0.158 × 0.047	0.2 × 0.1 × 0.05	0.2 × 0.17 × 0.15
Radiation	CuKα (λ = 1.54184)	Synchrotron (λ = 0.71073)	Synchrotron (λ = 0.71092)
2ϑ range for data collection (°)	8.792 to 150.58	3.572 to 64.194	3.924 to 55.13
Index ranges	-9 ≤ h ≤ 10, -13 ≤ k ≤ 12, -26 ≤ l ≤ 25	-16 ≤ h ≤ 16, -19 ≤ k ≤ 19, -30 ≤ l ≤ 30	-19 ≤ h ≤ 19, -16 ≤ k ≤ 15, -18 ≤ l ≤ 18
Reflections collected	30037	54041	35587
Independent reflections	7308 [R_{int} = 0.0686, R_{sigma} = 0.0526]	9238 [R_{int} = 0.0910, R_{sigma} = 0.0594]	6049 [R_{int} = 0.0828, R_{sigma} = 0.0494]
Data/restraints/parameters	7308/0/473	9238/329/542	6049/0/449
Goodness-of-fit on F^2	1.083	0.917	1.060
Final *R* indexes [$I \geq 2\sigma(I)$]	R_1 = 0.0732, wR_2 = 0.1970	R_1 = 0.0893, wR_2 = 0.2356	R_1 = 0.0456, wR_2 = 0.1286
Final *R* indexes [all data]	R_1 = 0.0804, wR_2 = 0.2122	R_1 = 0.1418, wR_2 = 0.2776	R_1 = 0.0503, wR_2 = 0.1330
Largest diff. peak/hole (e Å^{-3})	0.97/-0.67	1.14/-0.38	0.67/-0.56

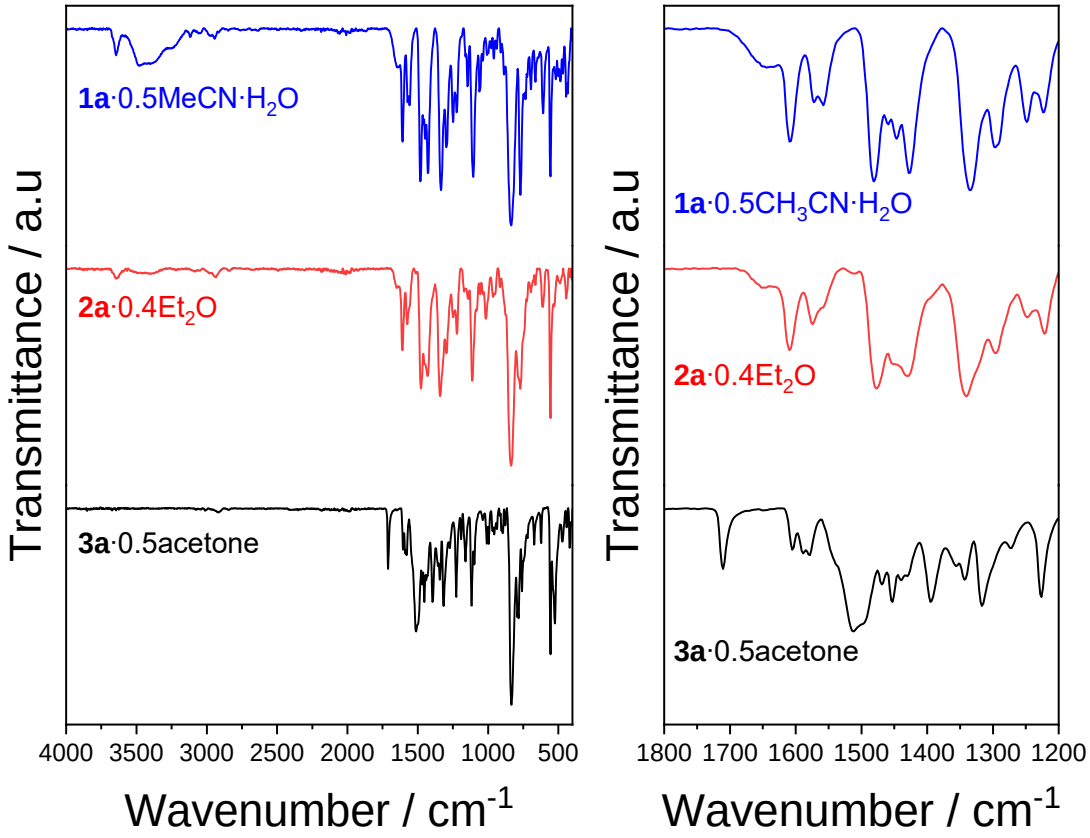

Fig S4 ATR-IR spectra of **1a**·0.5MeCN·H_2O, **2a**·0.4Et_2O and **3a**·0.5acetone in the region 4000 – 400 cm^{-1} (left) and 1800 – 1200 cm^{-1} (right).

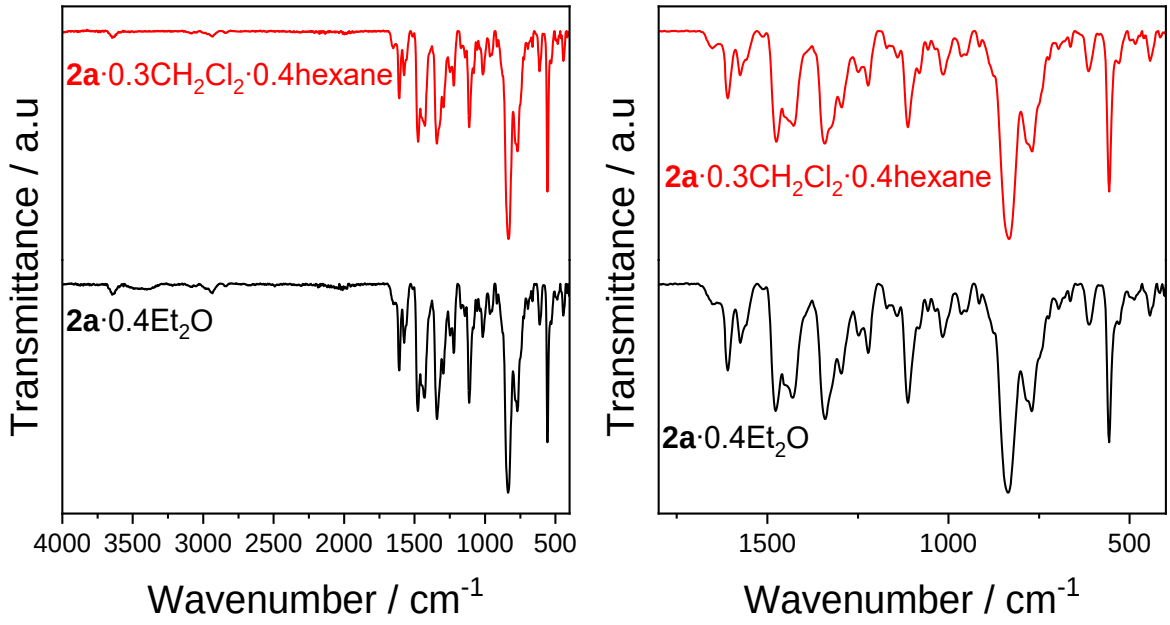

Fig S5 ATR-IR spectra of **2a**·0.4Et_2O and **2a**·0.3CH_2Cl_2·0.4hexane in the region 4000 – 400 cm^{-1} (left) and 1800 – 400 cm^{-1} (right).

Table S2 ATR-IR bands for compounds **1a**·0.5MeCN·H_2O, **2a**·0.4Et_2O and **3a**·0.5acetone.

Assignment	**1a**	**2a**	**3a**
ν(C=C)	1609 (s)	1609 (s)	1604 (s)
ν(C=C)	1572 (m)	1574 (s)	1588 (m)
ν(C=N)	1558 (m)	1559 (sh)	1578 (m)
ν(C-O) + δ(C-H)	1447 (s)	1441 (sh)	1512 (m)
ν(C-O) + δ(C-H)	1428 (s)	1430 (m)	1496 (sh)
ν(C-O/C-C/C=C)	1335 (s)	1339 (s)	1317 (m)
Skeletal diox	1296 (s)	1296 (m)	1273 (m)
ν(C-O/C-C)	1249 (s)	1248 (s)	1226 (s)
ν(C=O/C=C) + δ (C-H)	-	1453 (sh)	1469 (sh)
ν(P-F) – PF_6^-	835 (s)	835 (s)	835 (s)
ν(P-F) + δ(P-F) – PF_6^-	556 (s)	556 (s)	556 (s)

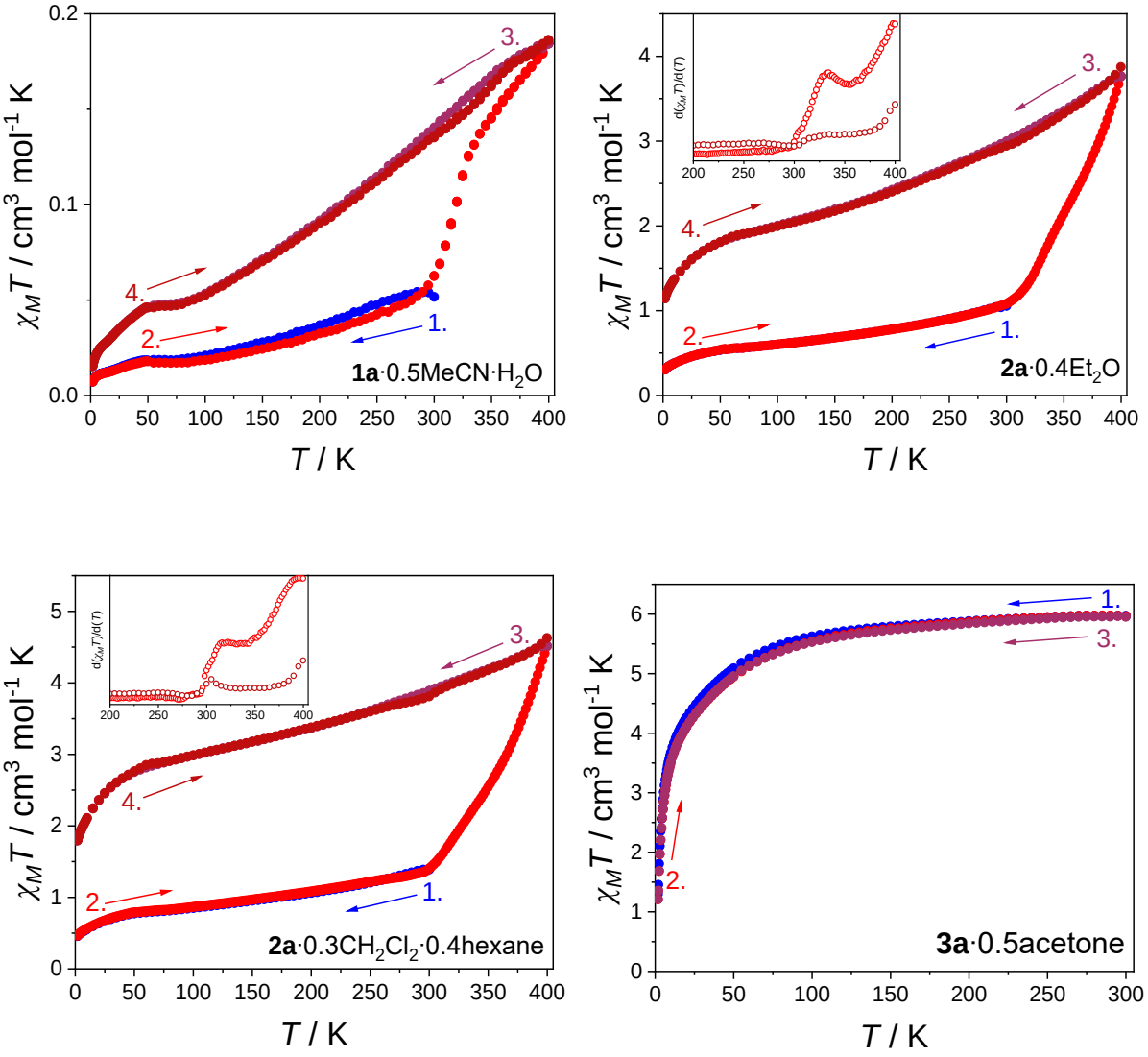

Fig S6 Plots of $\chi_M T$ vs T for **1a**·0.5MeCN·H$_2$O, **2a**·0.4Et$_2$O, and **2a**·0.3CH$_2$Cl$_2$·0.4hexane on first cooling 300 – 1.8 K (blue), first heating 1.8 – 400 K (red), second cooling 400 – 1.8 K (purple) and second heating 1.8 – 400 K (dark red). Plot of $\chi_M T$ vs T for **3a**·0.5acetone on first cooling (blue), first heating (red) and second cooling (purple). Number arrowed indicates the order and direction of the measurements. Inset for top right and bottom left: first derivative plot d($\chi_M T$)/d(T) for **2a**·0.4Et$_2$O (red) **2a**·0.3CH$_2$Cl$_2$·0.4hexane (blue) upon first heating (red) and second heating (dark red), highlighting the two-step VT behaviour and the plateau temperature.

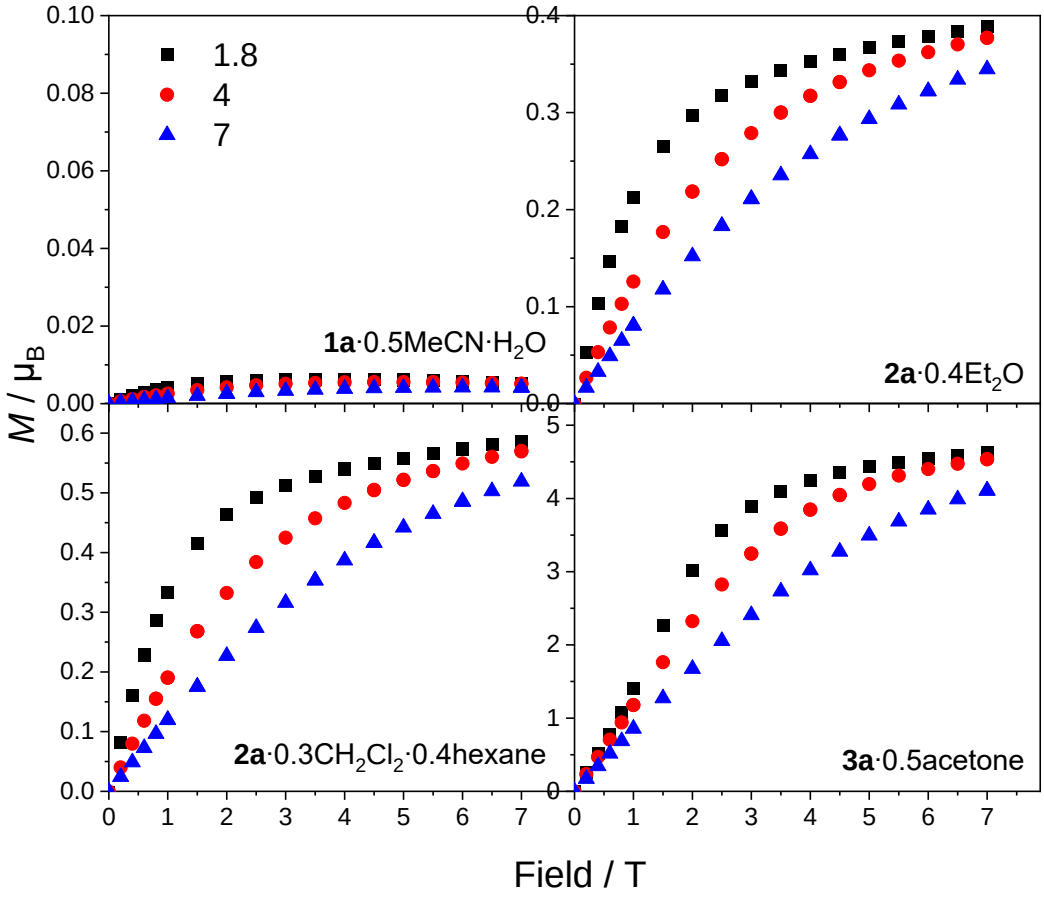

Fig S7 The field dependence of magnetisation for **1a**·0.5MeCN·H_2O, **2a**·0.4Et_2O, and **2a**·0.3CH_2Cl_2·0.4hexane and **3a**·0.5acetone at specified temperatures.

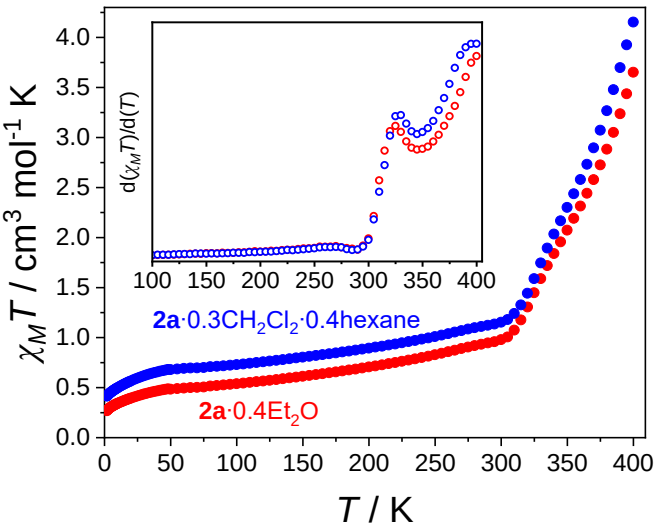

Fig S8 Plots of $\chi_M T$ vs T for **2a**·0.4Et$_2$O (red) and **2a**·0.3CH$_2$Cl$_2$·0.4hexane (blue) on heating 1.8 – 400 K. Inset: first derivative plot d($\chi_M T$)/d(T) for **2a**·0.4Et$_2$O (red) **2a**·0.3CH$_2$Cl$_2$·0.4hexane (blue) highlighting the two-step VT behaviour and the plateau temperature.

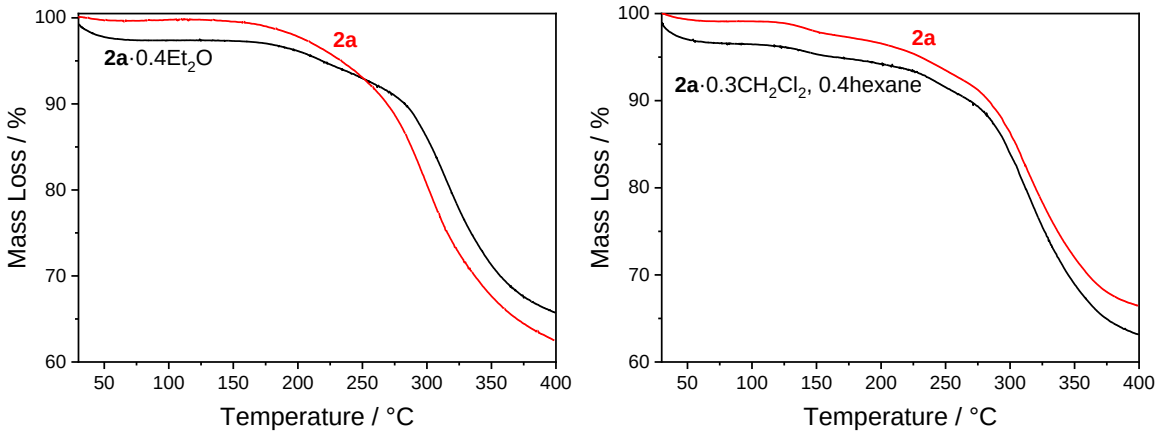

Fig S9 Thermogravimetric profile for **2a**·0.4Et$_2$O and **2a**·0.3CH$_2$Cl$_2$·0.4hexane before (black) and after (red) desolvation at a ramp rate of 5 °C min^{-1}.

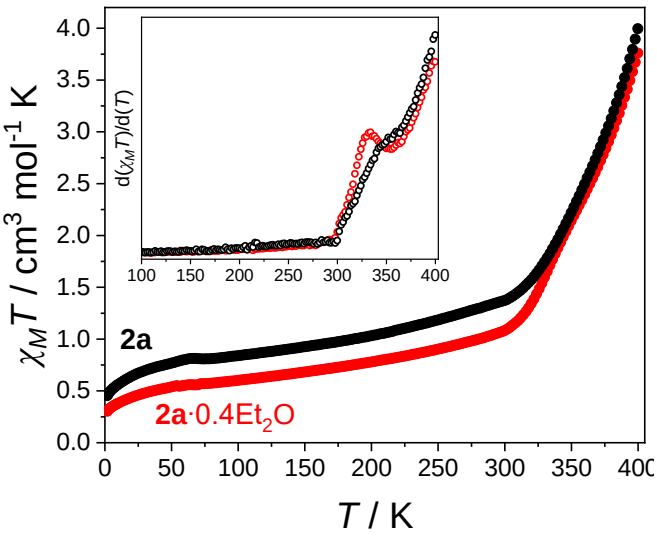

Fig S10 Plots of $\chi_M T$ vs T for **2a**·0.4Et$_2$O (red) and **2a** (black) on heating 1.8 – 400 K. Inset: first derivative plot d($\chi_M T$)/d(T) for **2a**·0.4Et$_2$O (red) **2a** (black) highlighting the two-step VT behavior and the plateau temperature.

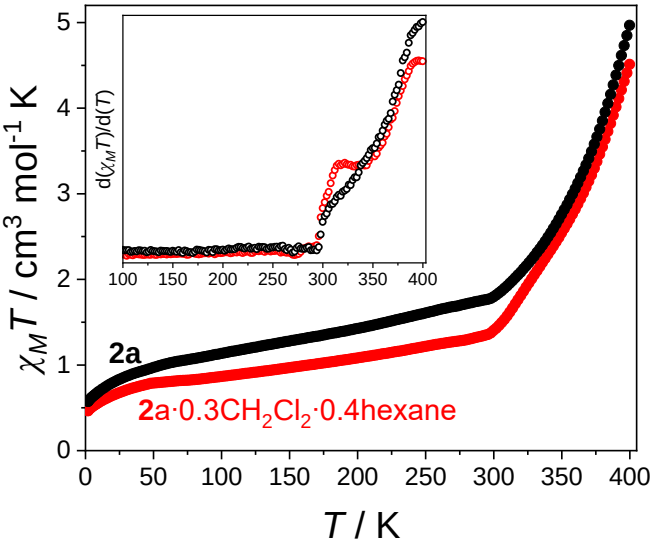

Fig S11 Plots of $\chi_M T$ vs T for **2a**·0.3CH$_2$Cl$_2$·0.4hexane (red) and **2a** (black) on heating 1.8 – 400 K. Inset: first derivative plot d($\chi_M T$)/d(T) for **2a**·0.3CH$_2$Cl$_2$·0.4hexane (red) **2a** (black) highlighting the two-step VT behavior and the plateau temperature.

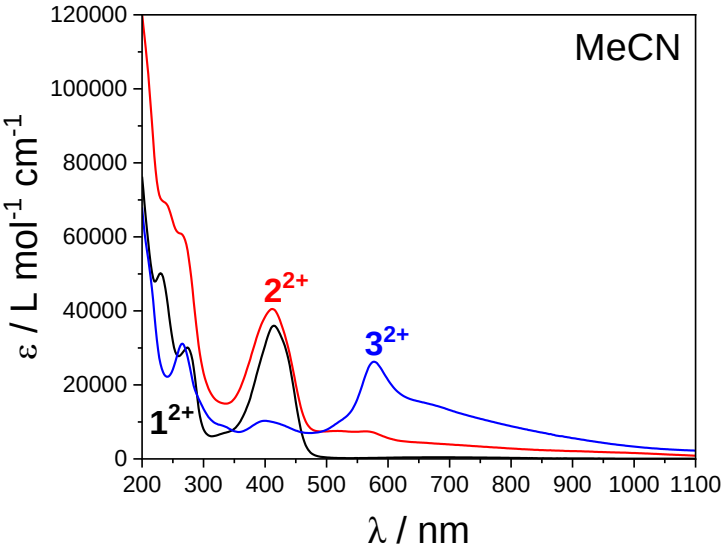

Fig S12 UV-Vis-NIR absorption spectra for MeCN solutions of $\mathbf{1}^{2+}$ (black), $\mathbf{2}^{2+}$ (red), and $\mathbf{3}^{2+}$ (blue) at 298 K.

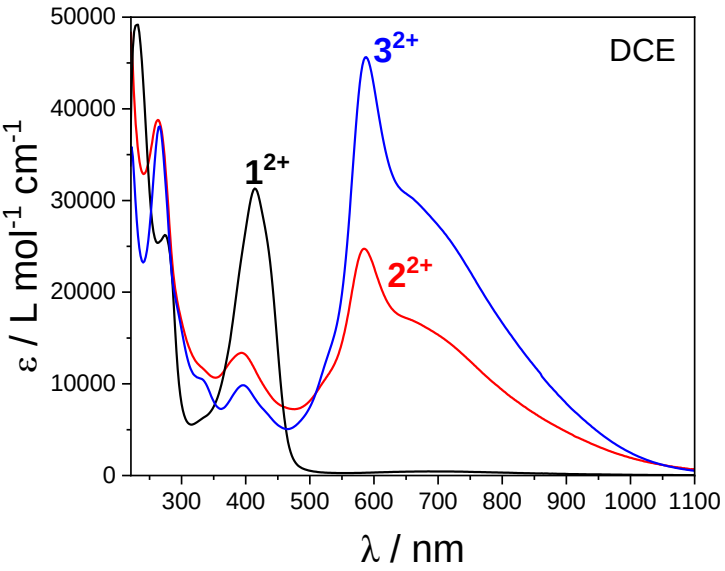

Fig S13 UV-Vis-NIR absorption spectra for DCE solutions of $\mathbf{1}^{2+}$ (black), $\mathbf{2}^{2+}$ (red), and $\mathbf{3}^{2+}$ (blue) at 298 K.

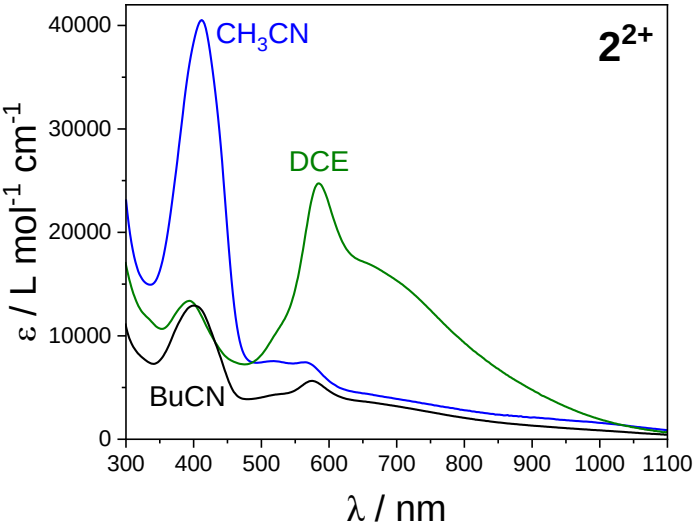

Fig S14 UV-Vis-NIR absorption spectra for MeCN (blue) and DCE (green) solutions of $\mathbf{2}^{2+}$ at 298 K.

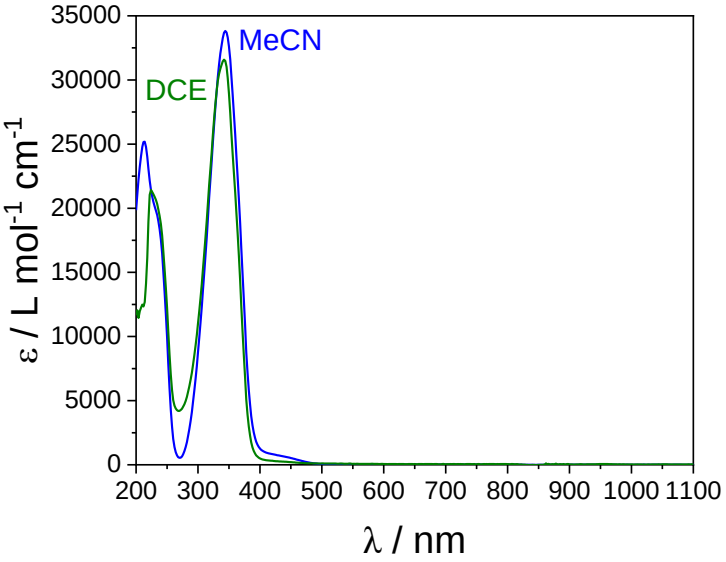

Fig S15 UV-Vis-NIR absorption spectra for MeCN (blue) and DCE (green) solutions of $thMH_4$ at 298 K.

Table S3 Electronic absorption bands for acetonitrile solutions of compounds $\mathbf{1}^{2+}$, $\mathbf{2}^{2+}$ and $\mathbf{3}^{2+}$.

Band assignment	λ / nm (ε / L mol^{-1} cm^{-1})
	$\mathbf{1}^{2+}$
$\pi - \pi^*$ cat^{2-}	232 (49937)
$\pi - \pi^*$	276 (29845)
LC cat^{2-}	418 (35607)
LMCT	684 (438)
	$\mathbf{2}^{2+}$
$\pi - \pi^*$ cat^{2-}	242 (68294)
$\pi - \pi^*$	266 (60808)
LC cat^{2-}	418 (39717)
LC SQ$^{\bullet-}$	522 (7532)
LC SQ$^{\bullet-}$	570 (9325)
LMCT	694 (4874)
	$\mathbf{3}^{2+}$
$\pi - \pi^*$	264 (31134)
MLCT	406 (10192)
LC SQ$^{\bullet-}$	580 (26122)
MLCT	704 (13011)

LC = ligand centered, LMCT = ligand to metal charge transfer, MLCT = metal to ligand charge transfer

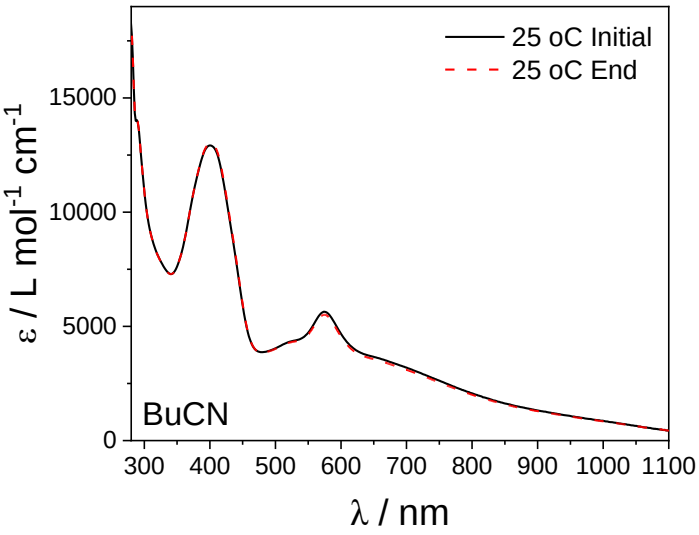

Fig S16 UV-Vis sample of $\mathbf{2}^{2+}$ BuCN at 298 K measured immediately following dissolution (black solid line) and after heating from 268 to 323 K.

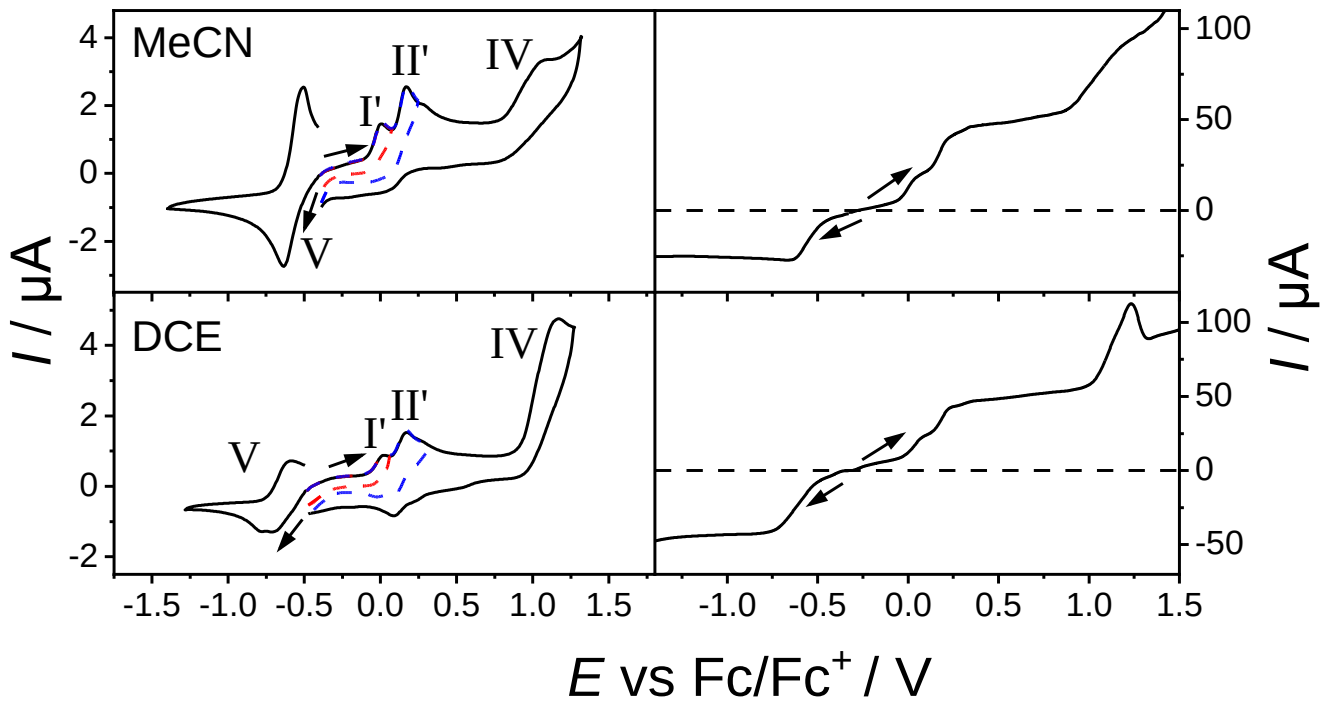

Fig S17 Cyclic voltammograms of MeCN or dichloroethane (DCE) solutions of compound $\mathbf{2}^{2+}$ (1.0 mM with 0.25 M Bu_4NPF_6) at a scan rate of 100 mV s^{-1} (left). Corresponding Rotating disc electrode voltammogram at a scan rate of 50 mV s^{-1} and a rotation rate of 500 rotations min^{-1}. Arrows indicate the starting potential and direction of the scan.

Table S4 Cyclic voltammetry and rotating disk electrode voltammetry data for compounds $\mathbf{2}^{2+}$ acetonitrile or 1,2-dichloroethane[a]

	Cyclic Voltammetry E_m or E_p / V (ΔE_p / mV)					Rotating Disk Electrode Voltammetry $E_{1/2}$ / V (i_L / µA)				
	I / I'	II / II'	III	IV	V	I / I'	II / II'	III	IV	V
2^{2+} (MeCN)	0.008[b]	0.155[b]	-	1.093[b]	-0.573 (130)	0.009 (20.9)	0.177 (42.6)	-	1.099 (97.3)	-0.528 (-27.2)
2^{2+} (DCE)	0.002 (75)	0.125 (90)	-	1.175[b]	-0.670 (160)	0.019 (11.6)	0.183 (21.4)	-	1.127 (56.1)	-0.595 (-21.0)

[a] 1.0 mM in MeCN or DCE, 0.25 M Bu_4NPF_6, scan rate 100 mV s^{-1}. Potentials reported vs Fc/Fc^+ couple. [b] E_p rather than E_m

Table S5 Cyclic voltammetry and rotating disk electrode voltammetry data for compounds **1a**, **2a** and **3a** and literature $[\{Co(Me_ntpa)\}_2(spiro)]^{2+}$ and $[\{Co(Me_ntpa)\}_2(Br_4spiro)]^{2+}$ complexes (n = 0, 2, 3)[1,2] in acetonitrile.[a]

	Cyclic Voltammetry E_m or E_p / V (ΔE_p / mV)					Rotating Disk Electrode Voltammetry $E_{1/2}$ / V (i_L / μA)				
	I / I'	II / II'	III	IV	V	I / I'	II / II'	III	IV	V
1a	0.070	0.17	-	0.98	-1.27[b]	0.08	0.22	-	1.02	-1.23
2a	0.01[b]	0.16[b]	-	1.09[b]	-0.57	0.01	0.18	-	1.10	-0.53
3a	-0.52	-0.66	0.25[b]	-	-	-0.49	-0.63	0.23		
$[\{Co(tpa)\}_2(spiro)](ClO_4)_2$	-0.15	-0.01	-	0.86	-1.11	-0.14	0.03	-	-	-
$[\{Co(Me_2tpa)\}_2(spiro)](ClO_4)_2$	-0.85	-0.71	0.00[b]	0.98[b]	-	-	-	-0.02	-	-
$[\{Co(Me_2tpa)\}_2(spiro)](PF_6)_2$	-0.86	-0.74	-0.08	1.14[b]	-	-0.88	-0.71	-0.01	-	-
$[\{Co(Me_3tpa)\}_2(spiro)](ClO_4)_2$	-0.86	-0.69	0.14[b]	-	-	-0.87	-0.68	0.17	-	-
$[\{Co(tpa)\}_2(Br_4spiro)](PF_6)_2$	0.17	0.30	-	1.09[b]	-0.993	0.18	0.33	-	1.10	-1.12
$[\{Co(Me_2tpa)\}_2(Br_4spiro)](PF_6)_2$	0.15[b]	0.31[b]	-	1.16[b]	-0.640	0.07	0.25	-	1.00	-0.66
$[\{Co(Me_3tpa)\}_2(Br_4spiro)](PF_6)_2$	-0.58	-0.42	0.29[b]	1.21	-	-0.61	-0.43	0.24	-	-

[a] 1.0 mM in MeCN, 0.25 M Bu_4NPF_6 or 0.1 M Bu_4NPF_6, scan rate 100 mV s^{-1}. Potentials reported vs Fc/Fc^+ couple. [b] E_p rather than E_m

Table S6 Separation of electrochemical processes for $\mathbf{1}^{2+}$, $\mathbf{2}^{2+}$ and $\mathbf{3}^{2+}$ in MeCN.[a]

	$\Delta diox$ / mV	$\Delta ox\text{-}red$ / mV
$\mathbf{1}^{2+}$	100	1340[b]
$\mathbf{2}^{2+}$	150 (125[c])	580[b] (670[c])
$\mathbf{3}^{2+}$	140	770[b]

[a]Calculated from CV potentials. Values reported to nearest 5 mV. [b]E_p used in calculations instead of E_m as potentials are irreversible. [c]DCE data

Table S7 Spin states (S), total energies without (E) and with (E^{ZPE}) zero-point harmonic vibrations, total enthalpies (H^{298}) and expectation values of the spin-squared operator ($\hat{S}^2$) of compounds **1a**, **2a** and **3a** as calculated by the DFT UTPSSh/6-311++G(d,p) method.

	Charge Distribution	S	E (a.u.)	E^{ZPE} (a.u.)	H^{298} (a.u.)	$\hat{S}^2$
1a	{Co^{III}-cat-cat-Co^{III}}	0	-7657.506788	-7656.538218	-7656.461501	0.000
	{Co^{III}-cat-SQ-Co^{II}}	2	-7657.491125	-7656.526360	-7656.447651	6.026
	βα[a]	1	-7657.488634	–	–	3.011
	{Co^{II}-SQ-SQ-Co^{II}}	4	-7657.468208	-7656.507571	-7656.428603	20.032
	αββα[a]	2	-7657.463563	–	–	8.001
	αααβ[a]	0	-7657.472389	–	–	3.806
	αβαβ[a]	0	-7657.467667	–	–	3.821
	αβαα[a]	3	-7657.470788	–	–	12.723
	βααα[a]	1	-7657.466049	–	–	5.017
2a	{Co^{III}-cat-cat-Co^{III}}	0	-7814.802502	-7813.724748	-7813.641633	0.000
	{Co^{III}-cat-SQ-Co^{II}}	2	-7814.798017	-7813.724225	-7813.639279	6.024
	βα[a]	1	-7814.796056	–	–	3.017
	{Co^{II}-SQ-SQ-Co^{II}}	4	-7814.788077	-7813.718246	-7813.630326	20.031
	αββα[a]	2	-7814.783714	–	–	7.954
	αααβ[a]	0	-7814.792190	–	–	3.816
	αβαβ[a]	0	-7814.788288	–	–	3.618
	αβαα[a]	3	-7814.790172	–	–	12.738
	βααα[a]	1	-7814.785386	–	–	5.024
3a	{Co^{III}-cat-cat-Co^{III}}	0	-7893.447036	-7892.313895	-7892.226750	0.000
	{Co^{III}-cat-SQ-Co^{II}}	2	-7893.452838	-7892.323799	-7892.234719	6.024
	βα[a]	1	-7893.451159	–	–	3.021
	{Co^{II}-SQ-SQ-Co^{II}}	4	-7893.449544	-7892.324574	-7892.235331	20.029
	αββα[a]	2	-7893.445821	–	–	8.023
	αααβ[a]	0	-7893.453678	–	–	3.809
	αβαβ[a]	0	-7893.450069	–	–	3.619
	αβαα[a]	3	-7893.451691	–	–	12.736
	βααα[a]	1	-7893.446888	–	–	5.026

[a] α corresponds to spin-up, β corresponds to spin-down; the order of the paramagnetic centers in {Co^{II}-SQ-SQ-Co^{II}}: (1) Co^{II} (2) SQ (3) SQ (4) Co^{II}

Table S8 Spin states (*S*), relative energies (Δ*E*), relative energies with zero-point harmonic vibrations (ΔE^{ZPE}), relative enthalpies (ΔH^{298}) (all values are given in kcal mol^{-1}) and the amount of spin density at the metal centres (q_s^{Co1}, q_s^{Co2}) of compounds **1a**, **2a** and **3a** as calculated by the DFT UTPSSh/6-311++G(d,p) method.

	Charge Distribution	*S*	Δ*E*	ΔE^{ZPE}	ΔH^{298}	q_s^{Co1}	q_s^{Co2}
1a	{Co^{III}-cat-cat-Co^{III}}	0	0.0	0.0	0.0	0.00	0.00
	{Co^{III}-cat-SQ-Co^{II}}	2	9.8	7.4	8.7	0.00	2.47
	{Co^{II}-SQ-SQ-Co^{II}}	4	24.2	19.2	20.6	2.47	2.47
2a	{Co^{III}-cat-cat-Co^{III}}	0	0.0	0.0	0.0	0.00	0.00
	{Co^{III}-cat-SQ-Co^{II}}	2	2.8	0.3	1.5	0.00	2.56
	{Co^{II}-SQ-SQ-Co^{II}}	4	9.1	4.1	7.1	2.57	2.57
3a	{Co^{III}-cat-cat-Co^{III}}	0	3.6	6.7	5.4	0.00	0.00
	{Co^{III}-cat-SQ-Co^{II}}	2	0.0	0.5	0.4	0.00	2.58
	{Co^{II}-SQ-SQ-Co^{II}}	4	2.1	0.0	0.0	2.59	2.59

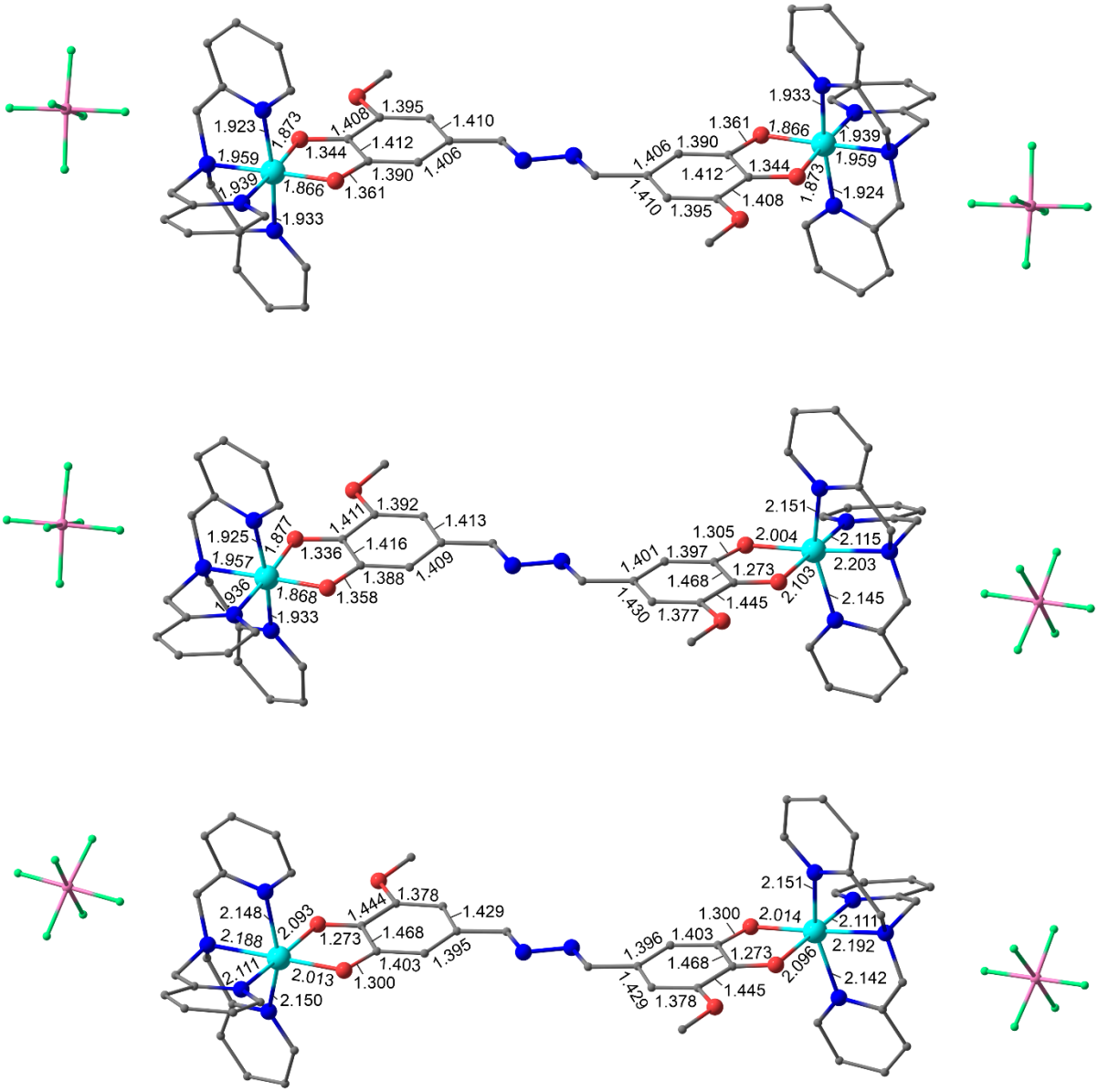

Fig S18 Optimized geometries of **1a** in the three charge distributions, {Co^{III}-cat-cat-Co^{III}} (top), {Co^{III}-cat-SQ-Co^{II}} (middle) and {Co^{II}-SQ-SQ-Co^{II}} (bottom) as calculated by the DFT UTPSSh/6-311++G(d,p) method. Hydrogen atoms are omitted; bond lengths are given in Å.

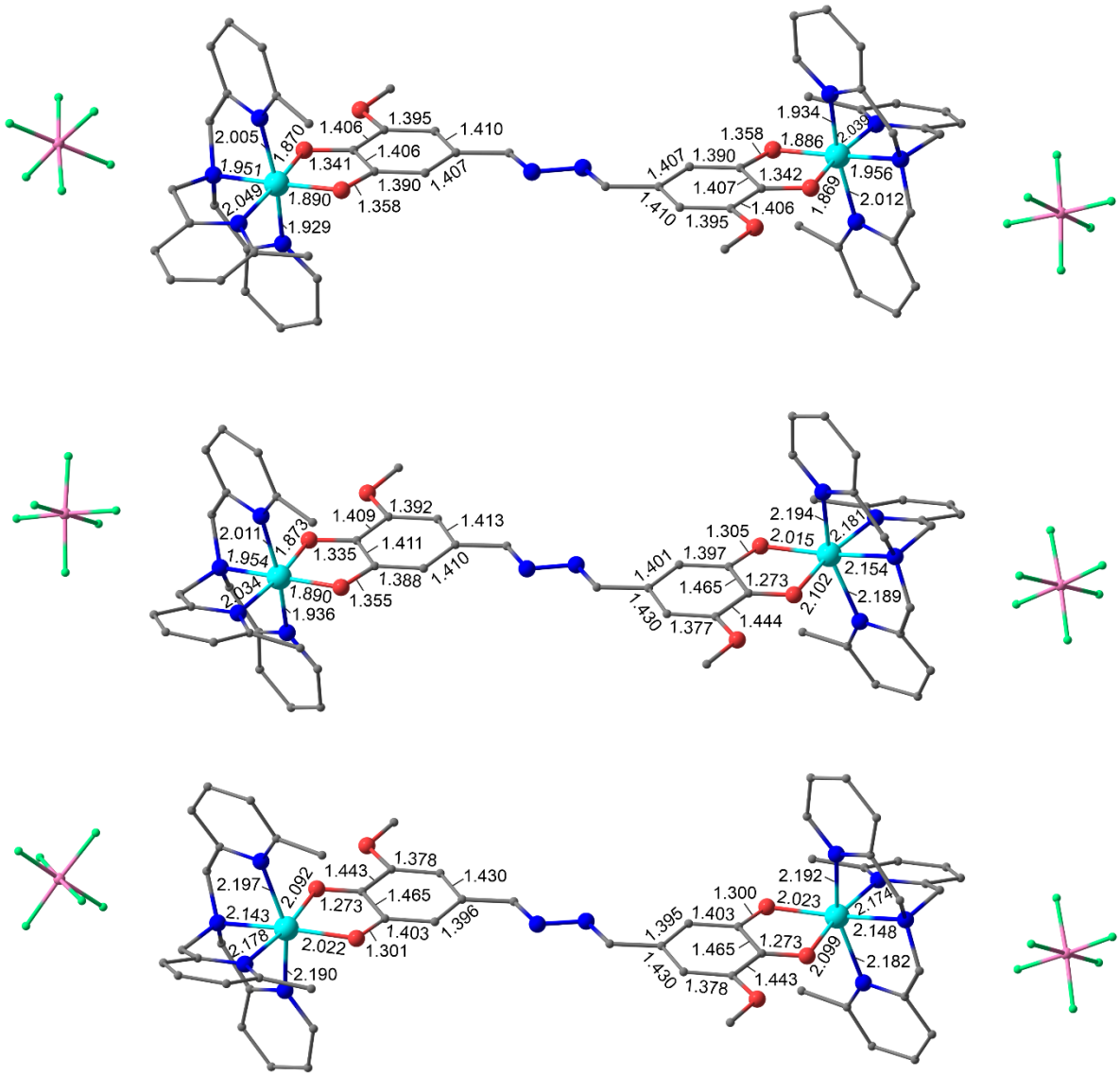

Fig S19 Optimized geometries of **2a** in the three charge distributions, {Co^{III}-cat-cat-Co^{III}} (top), {Co^{III}-cat-SQ-Co^{II}} (middle) and {Co^{II}-SQ-SQ-Co^{II}} (bottom) as calculated by the DFT UTPSSh/6-311++G(d,p) method. Hydrogen atoms are omitted; bond lengths are given in Å.

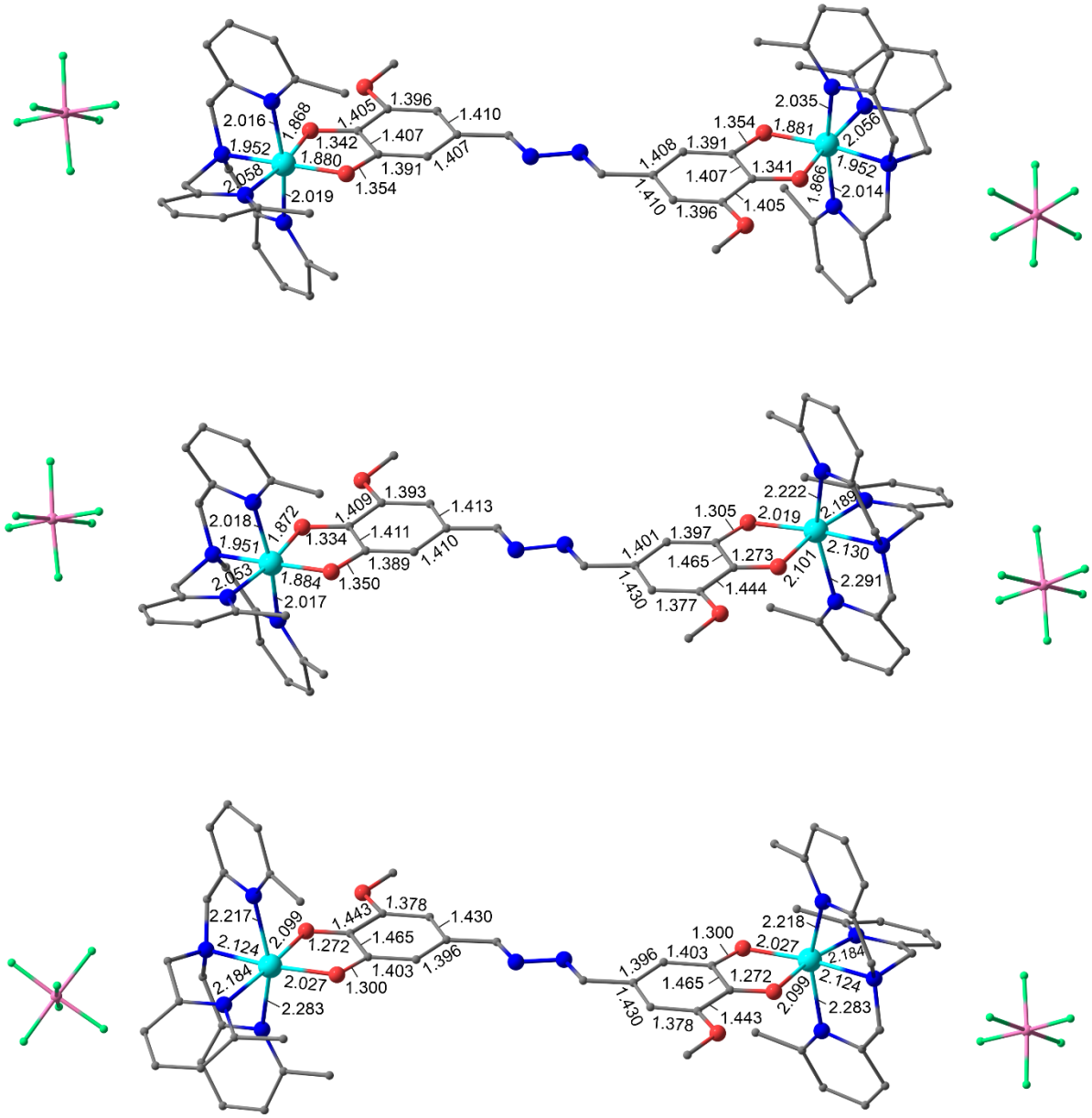

Fig S20 Optimized geometries of **3a** in the three charge distributions, {Co^{III}-cat-cat-Co^{III}} (top), {Co^{III}-cat-SQ-Co^{II}} (middle) and {Co^{II}-SQ-SQ-Co^{II}} (bottom) as calculated by the DFT UTPSSh/6-311++G(d,p) method. Hydrogen atoms are omitted; bond lengths are given in Å.

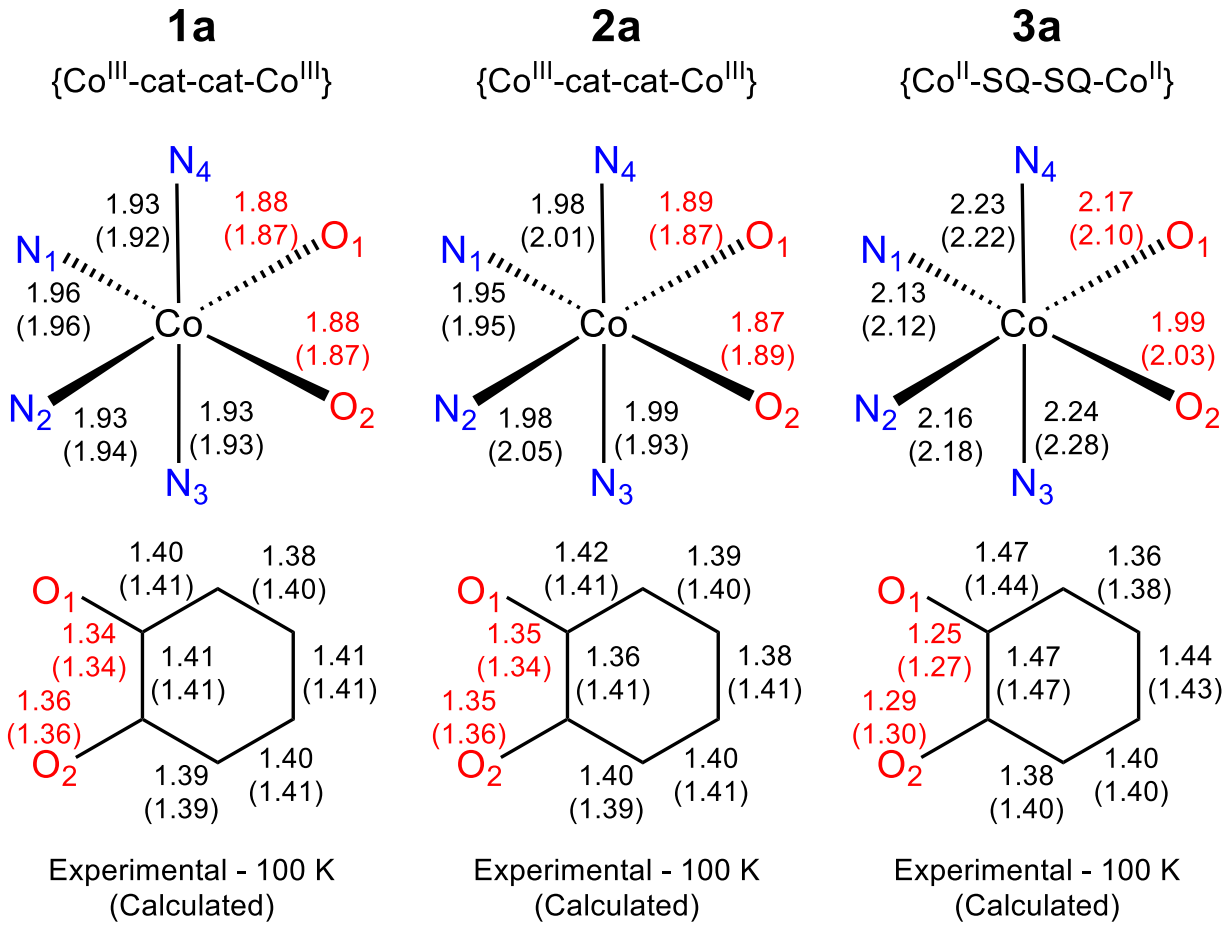

Fig S21 Comparison of the experimental bond lengths at 100 K for **1a**·2toluene·2MeCN, **2a**·1.8CH_2Cl_2, and **3a**·2acetone with the gas phase calculated bond lengths for the {Co^{III}-cat-cat-Co^{III}} state for **1a** and **2a** and {Co^{II}-SQ-SQ-Co^{II}} for **3a**. Experimental values listed above and calculated values listed below in brackets.

Table S9 Exchange coupling parameters (cm^{-1}) as calculated by the DFT UTPSSh/6-311++G(d,p) method.

Charge Distribution	Coupled moieties[a]	1a	2a	3a
{Co^{III}-cat-SQ-Co^{II}}	Co^{II}-SQ1	181	143	123
{Co^{II}-SQ-SQ-Co^{II}}	Co^{II}-SQ1	171	148	132
	Co^{II}-SQ2	–1	9	2
	SQ1-SQ2	–781	–782	–758
	Co^{II}-Co^{II}	7	5	7

[a] SQ1 represents the coordinated dioxolene and SQ2 represents the non-coordinated dioxolene.

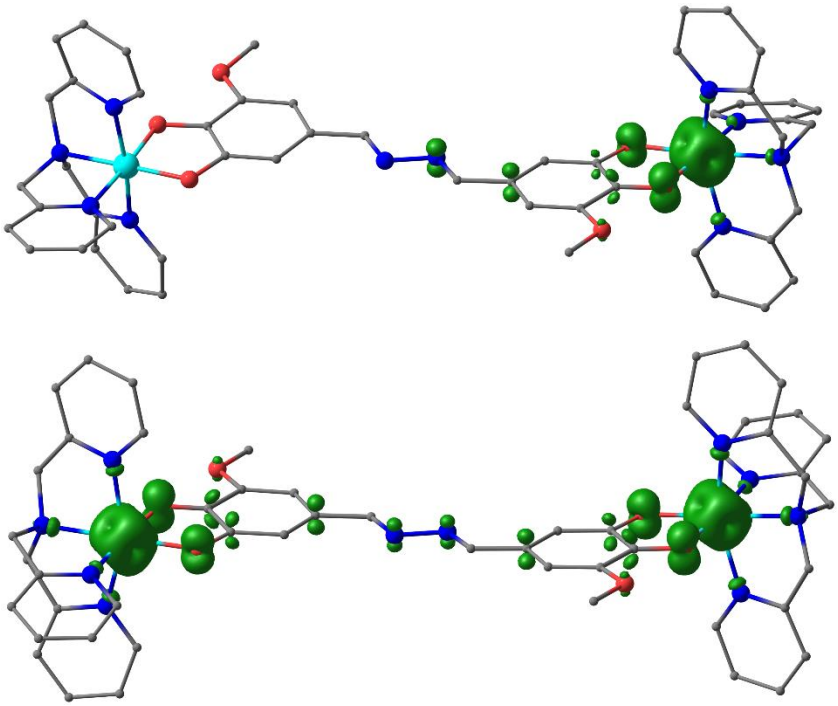

Fig S22 Spin density distribution (contour value = 0.015 e $Å^{-3}$) of the **1a** in the two charge distributions, {Co^{III}-cat-SQ-Co^{II}} (top) and {Co^{II}-SQ-SQ-Co^{II}} (bottom) as calculated by the DFT UTPSSh/6-311++G(d,p) method. Hydrogen atoms and PF_6^- anions are omitted.

References

1 G. K. Gransbury, B. N. Livesay, J. T. Janetzki, M. A. Hay, R. W. Gable, M. P. Shores, A. Starikova and C. Boskovic, *J. Am. Chem. Soc.*, 2020, **142**, 10692–10704.

2 K. G. Alley, G. Poneti, P. S. D. Robinson, A. Nafady, B. Moubaraki, J. B. Aitken, S. C. Drew, C. Ritchie, B. F. Abrahams, R. K. Hocking, K. S. Murray, A. M Bond, H. H. Harris, L. Sorace and C. Boskovic, *J. Am. Chem. Soc.*, 2013, **135**, 8304–8323.